IOP Publishing Physics in Medicine and Biology

Phys. Med. Biol. **52** (2007) 4827–4843 doi:10.1088/0031-9155/52/16/008

Non-invasive ultrasound-based temperature imaging for monitoring radiofrequency heating—phantom results

M J Daniels[1,2], T Varghese[1], E L Madsen[1] and J A Zagzebski[1]

[1] Department of Medical Physics, The University of Wisconsin–Madison, Madison, WI 53706, USA
[2] Department of Physics, The University of Wisconsin–Madison, Madison, WI 53706, USA

E-mail: mjdaniels@wisc.edu

Received 28 February 2007, in final form 22 May 2007
Published 30 July 2007
Online at stacks.iop.org/PMB/52/4827

Abstract

Minimally invasive therapies (such as radiofrequency ablation) are becoming more commonly used in the United States for the treatment of hepatocellular carcinomas and liver metastases. Unfortunately, these procedures suffer from high recurrence rates of hepatocellular carcinoma (∼34–55%) or metastases following ablation therapy. The ability to perform real-time temperature imaging while a patient is undergoing radiofrequency ablation could provide a significant reduction in these recurrence rates. In this paper, we demonstrate the feasibility of ultrasound-based temperature imaging on a tissue-mimicking phantom undergoing radiofrequency heating. Ultrasound echo signals undergo time shifts with increasing temperature, which are tracked using 2D correlation-based speckle tracking methods. Time shifts or displacements in the echo signal are accumulated, and the gradient of these time shifts are related to changes in the temperature of the tissue-mimicking phantom material using a calibration curve generated from experimental data. A tissue-mimicking phantom was developed that can undergo repeated radiofrequency heating procedures. Both sound speed and thermal expansion changes of the tissue-mimicking material were measured experimentally and utilized to generate the calibration curve relating temperature to the displacement gradient. Temperature maps were obtained, and specific regions-of-interest on the temperature maps were compared to invasive temperatures obtained using fiber-optic temperature probes at the same location. Temperature elevation during a radiofrequency ablation procedure on the phantom was successfully tracked to within ±0.5 °C.

(Some figures in this article are in colour only in the electronic version)

Introduction

The incidence of hepatocellular carcinoma (HCC) in the United States has increased significantly over the last two decades (Bosch *et al* 2004). In addition, it is one of the deadliest cancers with patient survival rates being less than a year without treatment after diagnosis. The number of cases of HCC has doubled in the United States in the last 20 years, and worldwide there are over 500 000 new HCC occurrences each year. Worldwide, HCC is now the fifth most common cancer in men and the eighth most common cancer in women. Due to hepatitis C infections (which lead to a 5% annual risk for liver cancer), the incidence rate of HCC in the United States and worldwide is expected to rise through to at least 2020 (El-Serag 2004, Wilson 2005).

Limitations of the two main methods of treating HCC, namely surgical resection and liver transplants, have led to the development of alternative treatment procedures. Most of these are minimally invasive procedures that destroy HCC tumors using either high temperature (at least 65 °C or higher (Heisterkamp *et al* 1999)) or freezing temperatures (−40 °C (Head and Dodd 2004)), without damaging surrounding healthy liver tissue. In some instances these treatments have increased the five-year survival rates of patients up to 59% (Wilson 2005). Radiofrequency (RF) ablation currently is the only FDA approved minimally invasive ablation therapy in the United States. RF ablation uses a probe with an active electrode tip or tips through which a 460–550 kHz alternating current is conducted. The current propagates through the body to grounding pads placed either on the back or the thigh of the patient. The conducted current causes ionic agitation and frictional heating (Head and Dodd 2004). Heat is then dissipated through thermal conduction to ablate the tumor, leading to temperatures of ∼100 °C in the tumor. Temperatures greater then 100 °C lead to tissue carbonization, leading to a loss of heat conduction and reduction in the size of the thermal coagulation.

Ultrasound is commonly used for guiding the insertion of the RF probe since it provides real-time and effective monitoring of needle insertion. As part of the post-procedure workup, CT scans are performed 48 h after treatment, to ascertain if the complete tumor was ablated. If viable residual cancerous tissue is detected on CT, it is necessary to reschedule the patient and reinsert the ablative electrode to perform additional treatment.

However, following probe insertion, ultrasound has not proven to be an effective method for determining the thermally coagulated region using B-mode imaging. For example, the ablated volume after the procedure can be either hypo-echoic, hyper-echoic or have the same echogenicity as prior to the RF ablation procedure (Gazelle *et al* 2000).

Therefore, other imaging modalities in addition to ultrasound have been pursued for guiding these minimally invasive treatments including CT and MRI (Merkle *et al* 1999, Hahn *et al* 1997). For real-time CT guidance, concerns regarding radiation for both patient and physician, and the amount of contrast agent that can be used (to avoid renal failure) limit the number of scans that can be performed. In addition, these procedures typically take up to 3 h, thereby increasing the cost associated with the procedure. Magnetic resonance imaging (MRI) of ablated regions reveal altered signal on both T1- and T2-weighted images (Goldberg *et al* 1998, Hyodoh *et al* 1998, Steiner *et al* 1997) with the treated areas devoid of gadolinium enhancement. However, only one manufacturer currently produces MR compatible RF ablation equipment, with the procedure requiring open MRI. MRI temperature imaging has also been performed following the insertion of the RF probe, but suffers from a lack of FDA-approved MRI-compatible RF probes, as well as from the much higher cost when compared to ultrasound (Carter *et al* 1998, Wacker *et al* 2004). MRI temperature imaging has also been used in conjunction with high-intensity focused ultrasound (HIFU) to treat tumors

in the uterus, liver and kidney in both humans and animals (Hindley *et al* 2004, Damianou 2004, Palussiere *et al* 2003).

The significant advantage with use of ultrasound-based methods such as elastography for thermal lesion delineation or temperature monitoring is that it can be performed on the patient in the surgical operating room, as opposed to moving the patient to the imaging system as is needed for use of MR or CT guidance (Merkle *et al* 1999, Hahn *et al* 1997). However, there is currently no clinically accepted method of temperature imaging using ultrasound. Several approaches have been proposed, including the tracking frequency shifts in the harmonics of the center frequency (Amini *et al* 2005), tracking attenuation changes (Worthington and Sherar 2001, Clarke *et al* 2003, Techavipoo *et al* 2004), measuring changes in backscattered energy (Arthur *et al* 2005b) and tracking shifts in the ultrasound echo signal due to thermal expansion and speed of sound (SOS) changes (Varghese *et al* 2002, Varghese and Daniels 2004, Techavipoo *et al* 2005, Arthur *et al* 2005a, Simon *et al* 1998).

The ultrasound-based temperature imaging method described in this paper (Varghese *et al* 2002, Varghese and Daniels 2004) utilizes accumulated echo shifts during thermal therapy, along with a single-valued displacement gradient-temperature calibration curve (Techavipoo *et al* 2005) that converts displacement gradients due to SOS changes and thermal expansion to temperature. Prior knowledge of the thermal expansion coefficient and the SOS change of the tissue with temperature are required to generate the calibration curve for this method of temperature tracking. Utilizing the calibration curve, Techavipoo *et al* (2005) were able to utilize speckle tracking algorithms such as 1D cross-correlation (CC) to track displacements and monitor temperature distributions.

In this paper, a well-characterized tissue-mimicking (TM) ultrasound phantom that can undergo repeated RF heating is used to test the accuracy of a temperature estimation algorithm that uses accumulated echo shifts and 2D CC-based algorithms. Accuracy of the method was determined by comparing estimated temperatures with temperatures obtained using invasive fiber-optic temperature probes placed within the phantom (gold standard). Our results show that 1D CC fails to track the displacement and, therefore, the temperature accurately; hence, 1D CC results are not included in this paper. 2D CC, on the other hand, was able to track tissue displacement in the phantom due to the heating procedure. The method yielded temperatures estimates within $\pm 0.5\ ^{\circ}$C of those measured invasively over the course of an 8 min RF heating procedure.

Materials and method

Tissue-mimicking phantom for temperature measurement

A thermal and acoustic tissue-mimicking (TM) phantom was constructed using material consisting of 1–2 mm diameter talc-in-agar spheres surrounded by a 10% *n*-propanol solution. The TM material has known thermal and acoustical properties (Chin *et al* 1990). Salt (NaCl) (0.6 g l^{-1}) was added to the phantom to make the electrical impedance of the TM material mimic that of the human body. A schematic diagram of the TM phantom apparatus is shown in figure 1, where (a) shows a side view of the phantom and (b) shows a view along the RF (radiofrequency) electrode. A central acrylic container is filled with the TM material and sits in a larger saline-filled container. Four 7 cm $\times$ 8 cm nylon mesh windows provide for thermal and fluid-flow contact of the TM material with the outside saline. The nylon mesh keeps the TM material confined to the central container and also allows access to the RF electrode and to the fiber-optic temperature probes. An RF ground exists below the container of the TM material. A RITA 1500 radiofrequency ablation electrode is fixed in the wall of the larger

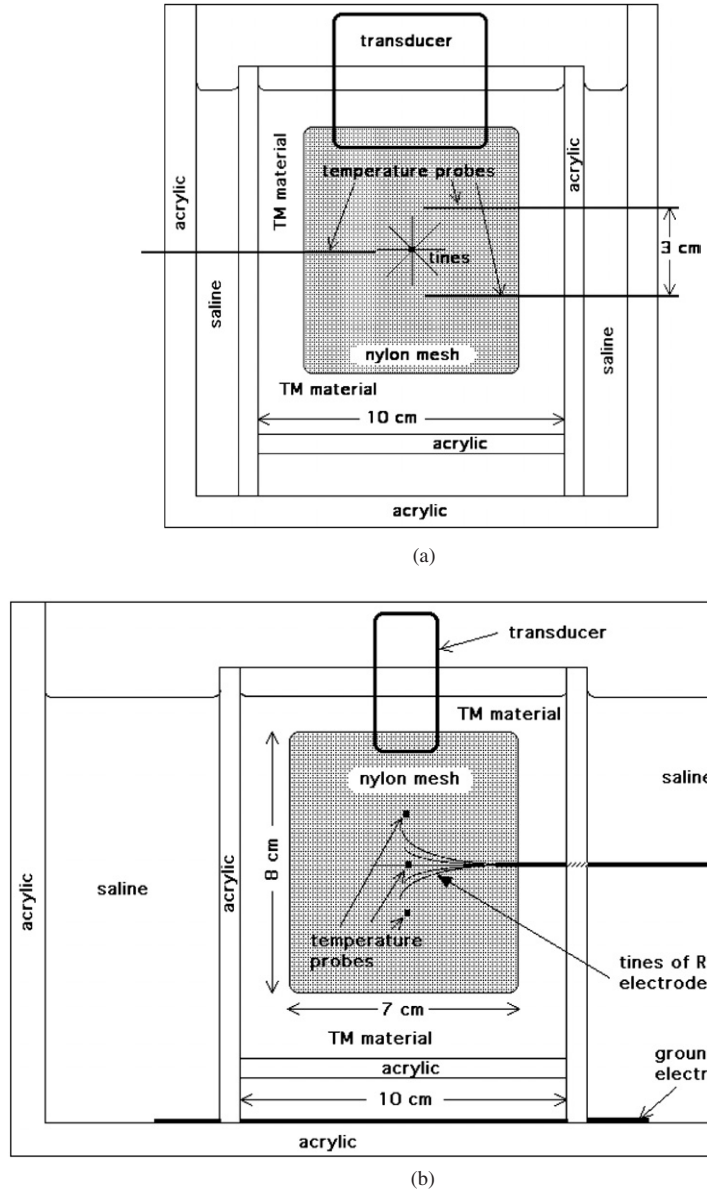

Figure 1. Schematic diagram of the TM phantom setup (not to scale) of the approximate locations of the RF ablation electrode and the fiber-optic temperature probes in the center of the inner container: (a) short side view and (b) long side view along the RF electrode.

saline-filled enclosure. The tines of the RF probe were extended in the middle of the TM phantom to lie within the ultrasound scanning plane. Three IPITEK (IPITEK, Carlsbad, CA) invasive fiber-optic temperature probes (blue and black wires in figures 2(a) and (b)) were placed near the ends of the extended electrode tines at the center of the phantom. These invasive probes serve as our temperature measurement 'gold standard.'

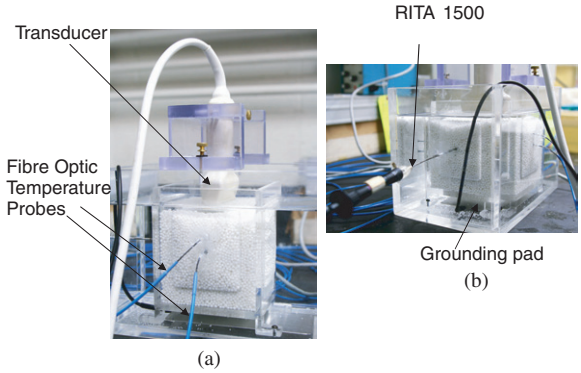

Figure 2. Photographs of the TM phantom setup (a) with the fiber-optic temperature probes and ultrasound transducer and (b) with the RF ablation electrode and grounding pad.

Invasive fiber-optic temperature measurement

The fiber-optic temperature probes apply a light pulse to a temperature-dependant fluorescent phosphor at the end of the probe. The fluorescent lifetime is temperature dependant, so by taking the ratio of the fluorescent intensities at two different time instances, we can solve for the fluorescent lifetime. This lifetime is related to temperature by utilizing a pre-computed lookup table generated from calibrated sources.

Spatial temperature distributions using ultrasound

Ultrasound data acquisition was performed using an Ultrasonix 500RP clinical ultrasound system equipped with a research interface (Ultrasonix Medical Systems, Redmond WA). A 1D linear array ultrasound transducer with a 6.6 MHz center frequency and 40 mm width was placed in contact with the TM material directly above the fiber-optic temperature probes and electrode tines. The ultrasound transducer has an approximate 60% bandwidth and the echo signals were digitized using a 40 MHz sampling frequency. The research interface on the ultrasound system provided radiofrequency echo signal frames as the phantom underwent an 8 min radiofrequency heating procedure. The maximum temperature generated in the TM phantom was approximately 65 °C, which is lower than the 100 °C temperature typically used for radiofrequency ablation of the liver. This was necessary to keep the phantom temperature lower than the 78 °C melting point of the talc-in-agar spheres. Invasive temperature values obtained using the fiber-optic probes were also recorded simultaneously during the heating procedure using a laptop computer connected to the fiber-optic temperature controller as shown in figure 3. The transducer, visible on the top surface of the phantom in figure 2(a), was held in place by a Lucite block to ensure that it remained stationary during the heating procedure. Radiofrequency echo data were recorded at a frame rate of approximately 1.25 frames per second, providing echo signals over an area of 6 cm (depth) × 5 cm (width) in the TM phantom.

Echo shifts (or apparent displacements) of the backscattered echo signals between two consecutive frames of radiofrequency echo data were then computed. Figure 4 shows a segment of the radiofrequency echo signal near the upper tine after 1 s and 60 s of ablation, respectively. Note the displacement in the radiofrequency echo signal with time. These shifts were tracked using a 2D cross correlation speckle tracking method (Zhu and Hall 2002). The

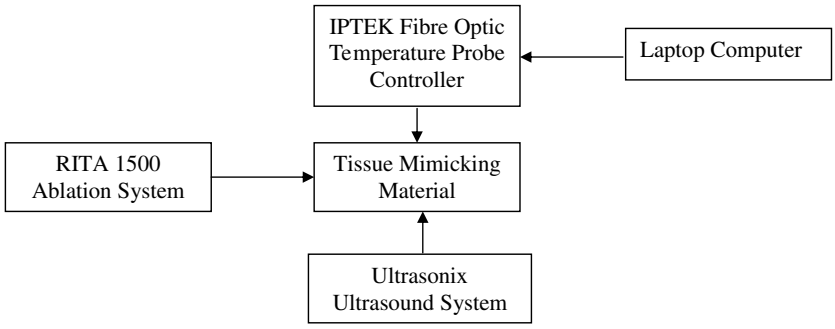

Figure 3. Diagram of the ultrasound system, radiofrequency ablation, fiber-optic temperature probe controller and laptop setup used for data collection.

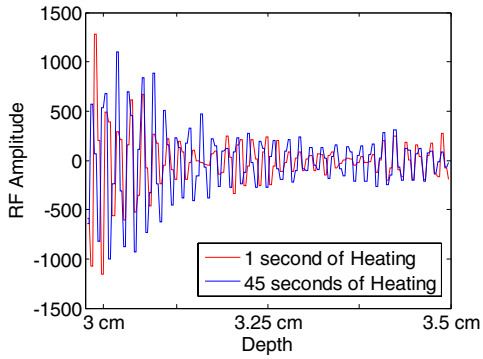

Figure 4. Radiofrequency echo data segment near the upper tine after 1 s (red) and 45 s (blue) of heating.

2D CC method relies on a modified block-matching algorithm developed for real-time strain imaging. The expression for the cross-correlation coefficient is given by

$$\mathrm{CC}(u, v) = \sum_{i=-(K_1-1)/2}^{(K_1-1)/2} \sum_{j=-(K_2-1)/2}^{(K_2-1)/2} [r_1(I+i, J+j) - r_2(I+i+u, J+j+v)]^2$$

where r_1 and r_2 are the pre- and post-heating RF echo fields, I and J are the axial and lateral RF indices representing the location of displacement estimation in the RF echo field, u and v represent the search location in the current search region, and K_1 and K_2 are the kernel's respective height and width. This method uses a predictive search algorithm that limits the search area of the tracking kernel based on the result of the previous displacement estimate. It also checks for consistency between displacement estimates before moving from one search row to the next. The input parameters to the 2D CC algorithm were the length of the gated A line (axial length of the kernel), kernel width and correlation technique namely block-matching or 2D CC. For the results shown in this paper, a window length of 4 wavelengths and lateral kernel width of 7 wavelengths was chosen.

The echo shifts were accumulated over the duration of the heating procedure. For example, the echo shift between 0 and 4 s of heating was first found, then the echo shift between 4 and 8 s of heating, etc. The total displacement for a spatial location from the start (0 s) of heating to the time of the current frame was accumulated. This process was continued until all the echo shifts over the entire 480 s of the heating procedure were obtained by accumulating the

frame-to-frame echo shifts, thereby tracking the motion trajectory. A 3 × 3 moving average filter was applied to the displacement data to help reduce noise artifacts. The gradient of the cumulative displacement was then computed using the linear least-squares approach, and a displacement gradient versus temperature calibration curve was applied to convert the gradient value into a temperature estimate, as discussed below.

Generation of the calibration curve

A calibration curve relating the gradient of the cumulative displacement to the TM material temperature was generated by combining the SOS changes of the material with temperature and its thermal expansion coefficient, using the following expression:

$$G(T) = \left(\frac{c_0}{c(T)}\right)(\delta d(T) + 1) - 1,$$

where $G(T)$ is the gradient of the displacement at temperature T, $\delta d(T)$ is the normalized material expansion given by $\delta d(T) = \frac{d(T)-d_0}{d_0}$, where $d(T)$ is the displacement due to thermal expansion at a given temperature, d_0 is the initial displacement, $c(T)$ is the SOS of the TM material at a given temperature, and c_0 is the SOS of the TM material at 25 °C. The expression for the gradient is the same as discussed by Techavipoo *et al* in generating a calibration curve for the liver from SOS and thermal expansion data (Techavipoo *et al* 2005). The theoretical derivation for this expression can be found in the previously mentioned work (Techavipoo *et al* 2005). The expression for the gradient of the displacement as a function of the SOS changes of the material with temperature and its thermal expansion coefficient is similar to that derived by Simon *et al* (1998). Since the TM material used is in slurry form and confined on all sides except the top, the volumetric expansion was used in the generation of the calibration curve. Additionally, the displacement due to thermal expansion of the TM material is toward the reference frame of the transducer. Therefore, from the transducers reference frame, the TM material appears to shrink instead of expand. This causes both the $\delta d(T)$ and the $c_0/c(T)$ term to be less than 1, resulting in a negative gradient from the transducer's reference frame. This results in a single-valued curve that relates a negative gradient (G) to the change in temperature as shown in figure 5(c) (Techavipoo *et al* 2005). A lookup table was then utilized to transform the gradient of the displacement to a temperature estimate.

The temperature dependence of the SOS of the TM material was measured using the substitution technique (Techavipoo *et al* 2002). The TM material was enclosed in a test cylinder, 2.5 cm thick and 7.6 cm in diameter with parallel 25 μm thick Saran Wrap transmission windows (Saran Wrap, Dow Chemical Company, Midland, MI). For measurements at 25 °C, 30 °C and 40 °C, degassed distilled water in the water bath was heated to the desired temperature using a pump and temperature controller (Haake, Karlsruhe, West Germany). The test cylinder was placed in the water bath for approximately 30 min in order to achieve thermal equilibrium. The sample was then placed perpendicular to the beam direction, between the transmitting and receiving transducers, and the change in propagation time with and without the test cylinder was recorded (Madsen *et al* 1999).

The transmitting transducer has a 5 MHz center frequency and diameter of 13 mm (Panametrics V309, Waltham, MA) and the receiving transducer (Aerotech Delta 2794-3, Krautkramer Inc., Lewistown, PA) has a 8 mm diameter. Both transducers used are unfocused. A function generator (Wavetek model 81, San Diego, CA) connected to a power amplifier (Amplifier Research model 75A250, Souderton, PA) was used to drive the transmitting transducer using 30-cycle duration narrowband pulses. The signal from the receiving transducer was displayed on a digital oscilloscope (LeCroy 9410, Chestnut Ridge, NY) and averaged over 50 successive transmitted pulses. The time shift in the received ultrasonic pulse

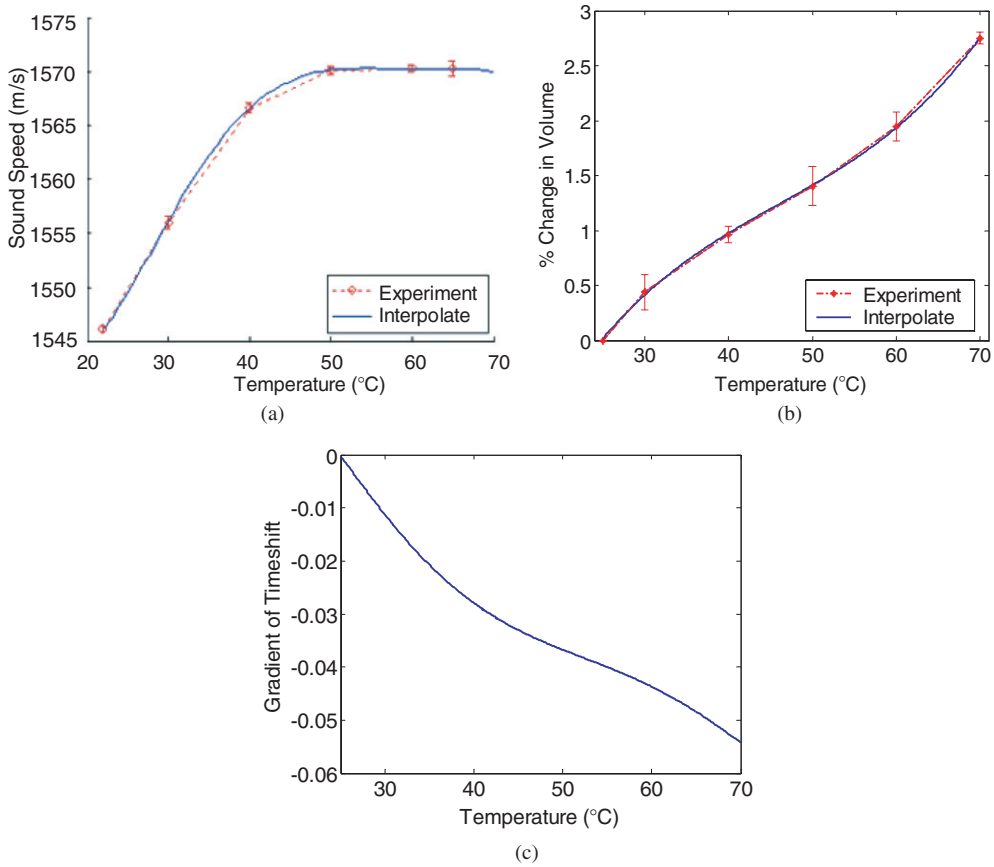

Figure 5. Derivation of the experimental calibration curve using the (a) SOS versus temperature plot, (b) normalized thermal expansion of water versus temperature and the (c) calibration curve that relates the gradient of the echoshifts to a change in the temperature.

after the cylinder was inserted between the transmit and receive transducers was recorded at the fifth zero crossing of the ultrasound pulse.

The SOS in the talc-agar spheres was then computed using: $c_m = c_w/(1 + c_w\Delta t/d)$, where c_m is the SOS of the talc-agar spheres at the specified temperature, c_w is the SOS of water at the specified temperature, Δt is the recorded time shift and d is the sample thickness. The SOS of water was estimated using a fifth-order polynomial (Greenspan and Tschegg 1959):

$$c_w = 3.0449 \times 10^{-9} \times T^5 - 1.452\,62 \times 10^{-6} \times T^4 + 3.136\,36 \times 10^{-4} \times T^3 - 0.057\,9506 \times T^2 + 5.033\,58 \times T + 1402.736,$$

where T is the temperature. At higher temperatures (50 °C, 60 °C and 65 °C), the measurement water bath was kept at 40 °C (in order to not damage the transducers) and the test cylinder containing the TM material was heated in a separate water bath to the desired temperature for approximately 30 min. The sample was quickly placed in the measurement bath, and the SOS measured. These SOS measurements were repeated ten times to obtain statistically significant results. The dependence of the SOS of the TM material on temperature is shown in figure 5(a), with an interpolated fit overlaid on the experimental data, and the fifth-order

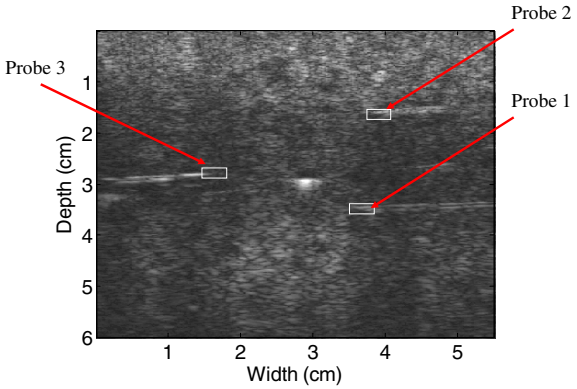

Figure 6. B-mode image illustrating the regions of interest (ROI) over which the temperature estimates obtained using 2D cross-correlation ultrasound-based temperature estimation and the measured fiber-optic probe temperature are compared.

polynomial fit is given by

$$SOS(T) = -8.3893 \times 10^{-7} \times T^5 + 0.000\,207\,81 \times T^4 - 0.019\,624 \times T^3 + 0.857\,95 \times T^2 - 16.209 \times T + 1652.1.$$

Volumetric thermal expansion values for the TM material was computed by placing 250 ml of the TM material in a KIMAX KG-33 (Kimble/Kontes Vineland, NJ) volumetric flask and measuring changes in the material volume at 25 °C, 30 °C, 40 °C, 50 °C, 60 °C and 70 °C, respectively. Care was taken to ensure that all air was removed from the flask prior to the experiment. The volumetric thermal expansion measurements were repeated ten times to obtain statistically significant results. The KIMAX flask has a volumetric thermal expansion coefficient of $96 \times 10^{-7}/°C$. Since this thermal expansion is $\sim 1/1000$ of the thermal expansion of the TM material, it was ignored for the purposes of this experiment (Weast 1978). Figure 5(b) presents the per cent change in the volume of the TM material as a function of temperature for the experimental data. A third-order polynomial fit to the experimental data is given by

$$\text{Per cent change } (T) = 3.5519 \times 10^{-7} \times T^3 - 4.8986 \times 10^{-5} \times T^2 + 0.002\,6786 \times T - 0.041\,743.$$

The per cent change in volume of the TM material is close to the per cent change in the volume of water (3.3% from 25 °C to 70 °C) (Weast 1978). This is as expected since the TM material is approximately 88% water and is surrounded by a solution that is 90% water. The per cent change in the volume of the TM material was used to generate the calibration curve as discussed above.

Results

Figure 6 shows an ultrasound B-mode image of the TM phantom that includes a cross-section of the radiofrequency electrode tines along with the invasive fiber-optic probes used to measure temperature. It should be noted that only the center tine is visible in this B-mode image. The outer tines were not visible in the B-mode image, unless they were moved. This is expected since the size of the tines (0.534 mm) is on the order of the PSF of the Ultrasonix transducer

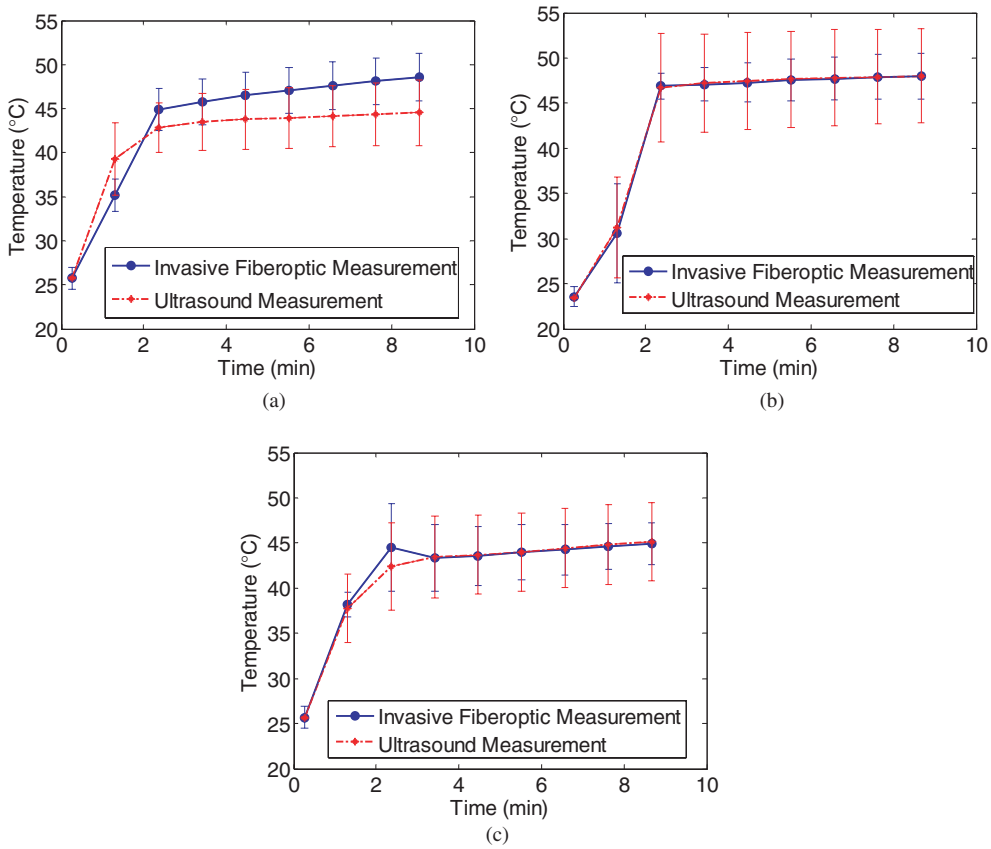

Figure 7. Quantitative comparison of the temperature using ultrasound-based temperature estimation and fiber-optic temperature measurements. The blue curve denotes the ideal fiber-optic probe temperature measurement computation and the red curve the ultrasound-based temperature measurement. Displacement data were accumulated from radiofrequency echo data accumulated every 2.5 s for ROIs at the (a) probe 1 (lower right side), (b) probe 2 (upper right side) and at the (c) probe 3 (lower left side). The error bars are shown only for limited estimates to reduce the clutter in the graph.

at 6.6 MHz. In figure 6, three 34 mm $\times$ 19 mm ROIs are highlighted to demonstrate areas that were selected around the three fiber-optic temperature probes for comparison of the temperature estimated non-invasively using ultrasound and the temperature measured using the 'gold standard' fiber-optic temperature probes. The mean and standard deviation of the temperature derived from ultrasound were compared to the temperature obtained using the fiber-optic probes for ten independent experiments. Figure 7 presents results obtained during the heating procedure, where only selected data points and error bars are shown to reduce clutter on the graphs for a separation of five frames between displacement accumulations. Figure 7(a) compares invasive fiber-optic temperature measurements of probe 1 to those obtained using non-invasive temperature estimates in the ROI surrounding probe 1. The ultrasound ROI-based temperature result is lower than that of the fiber-optic probe, but within one standard deviation for all time steps. In a similar manner, figure 7(b) compares the fiber-optic temperature measurement result of probe 2 to that obtained in the ROI around probe 2.

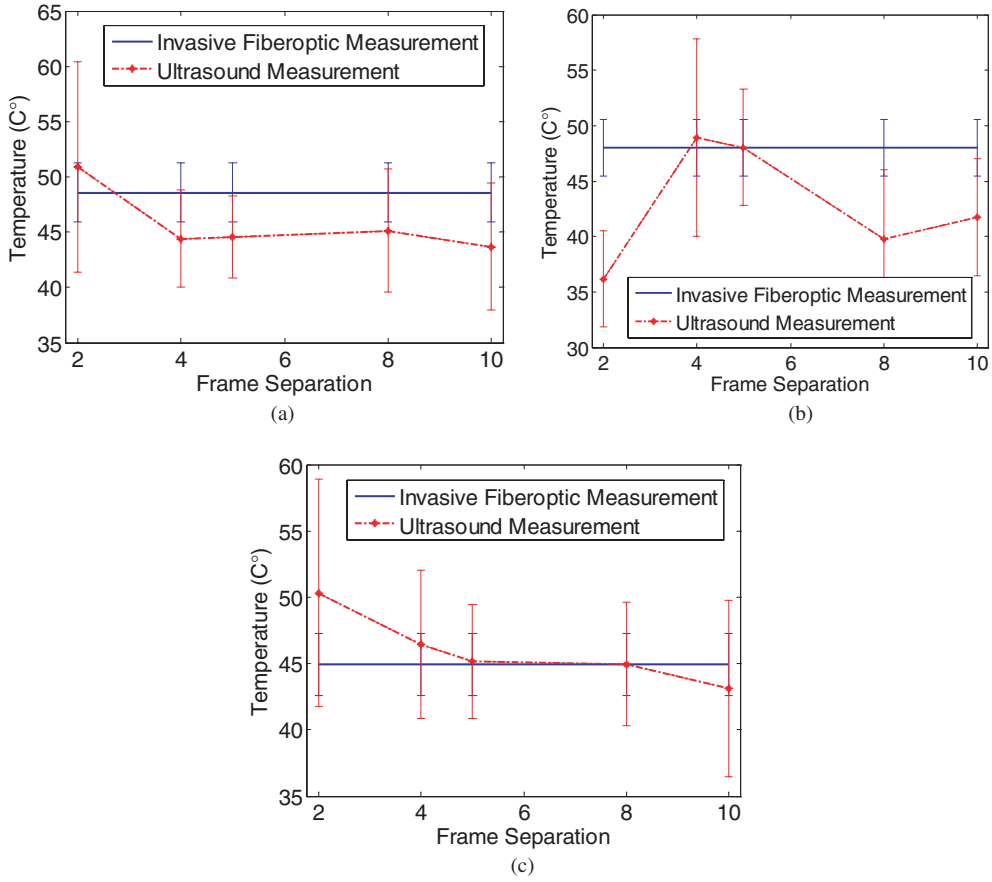

Figure 8. Quantitative comparison of the temperature estimated using ultrasound-based temperature estimation and temperature recorded using the fiber-optic probes for different frame separations over the heating duration. In (a), (b) and (c) the blue curve denotes the 'gold standard' fiber-optic temperature measurement, while the red curve denotes the ultrasound-based temperature estimated in the ROI around (a) probe 1, (b) probe 2 and (c) probe 3.

The average temperature estimated in probe 2's ROI from the ultrasound echo shifts is within ±0.5 °C of that of the average fiber-optic measurement for all time steps. This result may be a little misleading since the experimental error is greater than ±0.5 °C for the fiber-optic temperature probes. It should be noted that the standard deviation for ultrasound temperature estimations within the ROI for probe 2 is approximately 1 °C higher than the standard deviations of the temperature estimates obtained for probes 1 and 3. Finally, figure 7(c) compares the invasive fiber-optic temperature measurement of probe 3 to that obtained in the ROI around probe 3. For probe 3, the average ultrasound-based ROI temperature measurement is within ±0.5 °C of that obtained using the fiber-optic temperature probe (one temperature estimate was an outlier with a standard deviation of 2.18 °C). The maximum amount of separation between two mean temperature measurements on any of the graphs was 4 °C, and the mean separation of the temperature estimates from all of the graphs is ±1 °C. When taking the standard deviations into account the maximum difference was ±5 °C.

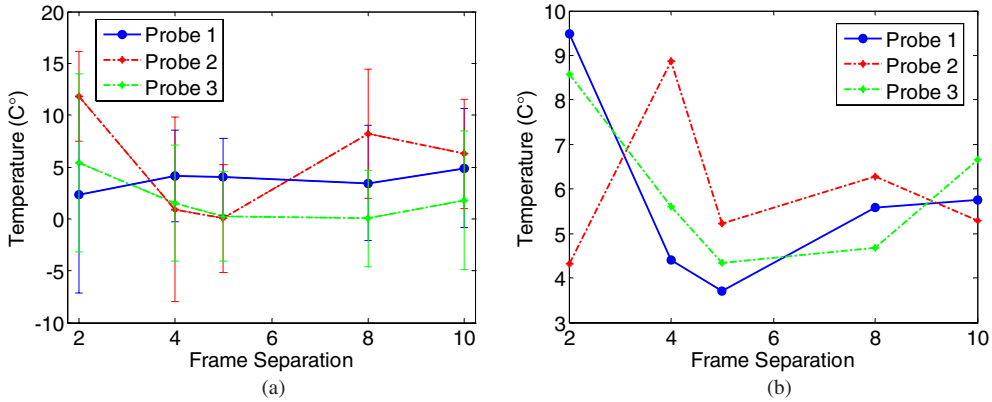

Figure 9. The temperature measurement differences between the mean temperature recorded using the fiber-optic probe and the mean ultrasound-based temperature measurements in the corresponding ROI are plotted in (a) for all three probes and (b) where the standard deviation versus the frame separation for all the three probes are shown.

Figure 8 presents a comparison of the invasive 'gold standard' temperature measured using fiber-optic probes and ultrasound-based temperature estimated using radiofrequency frames separated by different frame separation intervals. This figure presents the tradeoffs associated between reducing computational time by using large frame separations with the possibility of trying to estimate frame-to-frame displacements that are too large to track. Any frame-to-frame displacement errors will affect the accuracy of the temperature estimation. For instance, a frame separation of two frames indicates that local displacements are calculated (and accumulated) between frames 1 and 3, 3 and 5, etc, over the entire 480 s and 700 frames acquired during the heating procedure. Frame separations of 2, 4, 5, 8 and 10 frames were examined to compute the optimum frame separation that would provide an ultrasound-based temperature estimate that was closest to the fiber-optic temperature measurement. Figure 8(a) presents the comparison results for probe 1, figure 8(b) for probe 2 and finally figure 8(c) for probe 3. The results in figure 8 illustrate that a frame separation of five frames provides temperature estimates that are closest to the temperature measured using the fiber-optic probe with the 2D cross-correlation method. A frame separation of five frames was used to calculate the rest of the results presented in this paper.

Figure 9(a) plots the absolute difference between the mean fiber-optic temperature measurement and the mean ultrasound-based temperature estimated within the ROI, while figure 9(b) presents its standard deviation. From figures 9(a) and (b) it is clear that for probes 2 and 3 both the lowest standard deviation and the smallest difference between the two temperature measurements occur at a frame separation of five frames. For probe 1, the lowest standard deviation occurs at a frame separation of five frames, but the difference between the ultrasound-based temperature estimates and fiber-optic temperature measurements do not change significantly with different frame separations.

In figure 10, non-invasive ultrasound-based 'displacement maps' are shown. These displacement maps indicate local apparent displacements (in mm) of the material within the TM phantom after 45 s, 90 s, 180 s and 360 s of heating, respectively. The ROI used for the fiber-optic probe temperature estimates are outlined in the images at the locations mentioned above. For each map the apparent displacements are observed to increase from the bottom to the top surface of the phantom. This is an interesting result because the tines

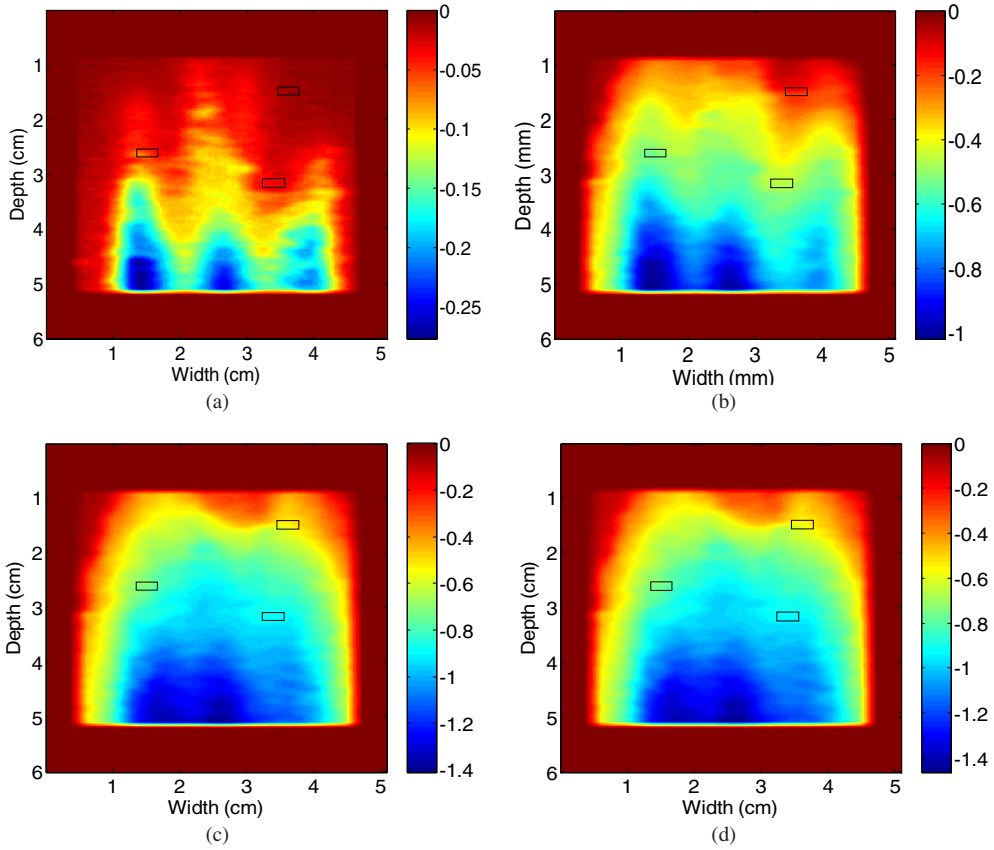

Figure 10. Ultrasound-based displacement maps (in mm) after (a) 45 s, (b) 90 s, (c) 180 s and (d) 360 s of RF heating.

of the radiofrequency ablation electrode are exactly at the center of the region represented by the temperature image, so one would expect the displacement associated with regions near the upper tines to be toward the top and those near the lower tines to be toward the bottom of the phantom.

The reason for this asymmetry is likely due to the fact that the top of the TM material container is open or unconstrained, while the bottom and sides have a fixed mesh boundary. Thus, the predominant expansion of the TM material is toward the top surface of the phantom in these experiments. Taking the gradient of these displacements in the direction of the ultrasound beam propagation leads to the temperature maps shown in figure 11 at (a) 45 s, (b) 90 s, (c) 180 s and (d) 360 s of heating. In this figure, the temperature is observed to increase toward the top of the container with an increase in the duration of RF heating. As in figure 10, the ROIs used for the fiber-optic probe temperature estimates are outlined in the images. It should be noted that the highest temperatures in figures 11(c) and (d) occur at the top of the container. This is probably due to the large displacement gradient near probe 2 (figures 10(c) and (d)), leading to the high temperatures in this area (figures 11(c) and (d)). In addition, these temperature maps were able to estimate probe 2's (which lies in this area) temperature to within ± 0.5 °C. Therefore, the high temperatures indicated by ultrasound measurements in this area seem to be correct.

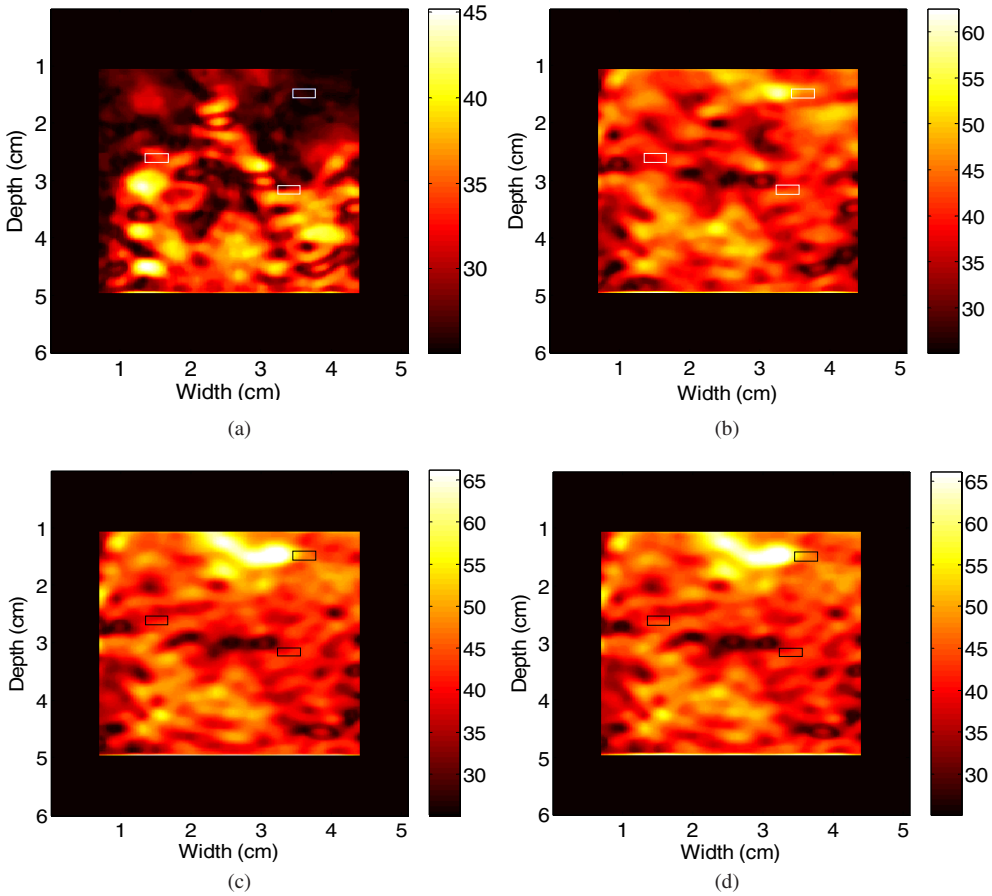

Figure 11. Ultrasound-based temperature maps after (a) 45 s, (b) 90 s, (c) 180 s and (d) 360 s of RF heating.

Two other factors may also contribute to the apparent displacement patterns moving toward the transducer. First, since the ground pad is placed close to the ablation needle in this experiment, the lower electrodes partially block the current emanating from the upper electrodes. This leads to the lower electrodes reaching a higher temperature before the upper electrodes. This effect was seen experimentally in all ten of the acquired data sets. Secondly, as the TM slurry is heated, convection currents may arise that may cause the warmer water between talc spheres near the bottom of the container to move upward, further leading to an apparent upward displacement of the heated material. However, this effect is likely to be small since the temperature difference overall between the top and bottom of the container is small, and no large-scale upwelling of the spheres was observed in B-mode images also acquired during the experiments.

Discussion and conclusion

Minimally invasive therapies are being used with greater regularity in treating HCC and liver metastases. RF ablation is the most commonly used minimally invasive therapy for treating

HCC. However, the effectiveness of RF ablation is limited by the fact that there are no FDA-approved and cost-effective methods to obtain real-time temperature maps during the ablation procedure. The lack of feedback to the clinician during the ablation procedure may contribute to the increased recurrence rate of HCC following ablation therapy. This in turn leads to repeat ablation procedures and undue stress and cost to the patient. In this paper, we demonstrate that real-time temperature imaging can be performed in a TM phantom using ultrasonic methods. Ultrasound is the most commonly used method of monitoring RF probe placement, so this work is a step toward using this modality to provide real-time feedback during ablation therapy. This could provide the physician with additional information to determine if the entire tumor has been successfully ablated. Future work will examine the effectiveness of our temperature estimation method in *in vitro* liver tissue and *in vivo* on animal models.

The non-invasive temperature imaging results obtained by heating the TM phantom are promising and demonstrate that a calibration curve can be generated for the material as long as the material SOS variation with temperature and its thermal expansion are known. However, similar experiments involving fiber-optic temperature probes and liver tissue must be performed to ensure that the level of accuracy achieved in this experiment can be carried over to *in vivo* situations.

In this experiment, we were able to obtain ultrasound-based temperature estimates to within ± 0.5 °C for two of the three fiber-optic probes and within ± 5 °C for all the fiber-optic temperature probes. A frame separation of five frames was found to provide the most accurate and precise temperature estimates using the 2D cross-correlation method to estimate local displacements. This is promising given that there might be several sources of error in our displacement and thereby the temperature estimates. Firstly, although the fiber-optic temperature probes are visible in the ultrasound B-mode images, the probes are quite flexible and the tips of the probes (where the temperature is measured) could be displaced or tilted slightly to the sides of probe locations indicated by the B-mode images, leading to a different temperature reading from that determined using echo time shifts. This could account for the ultrasound-based estimates of the ROI around probe 1 being consistently different than the measured fiber-optic temperature.

For instance, probe 1 was located between the center tine of the RF electrode and a side tine of the RF electrode. If the tip of probe 1 was slightly displaced toward the tip of the tines, then it would lead to a higher fiber-optic temperature measurement than the ultrasound-based temperature estimation. The reverse is true if the tip of probe 1 is farther from the tip of the electrodes. This is true in figure 7(a), except for the initial temperature measurement, since the start temperature was 25 °C for both the calibration curve and the experimental setup. Therefore, the initial temperature for both the fiber-optic temperature probes and the ultrasound temperature estimates are expected to be $\sim$25 °C, which they are. Our conclusion that the tip of probe 1 was outside the imaging plane is further backed up by figure 9(a), since the difference between the ultrasound-based temperature estimate and temperature measured using the fiber-optic probe remains unchanged with different frame separations.

Secondly, the ultrasound scan plane has a thickness much greater than that of the fiber-optic temperature probe tip, leading to a volume averaging effect on the temperature estimated. This volume averaging could lead to either overestimation or underestimation of the temperature, depending on whether the temperature at the tine is significantly lower or higher, respectively, than the surrounding scan plane under the ultrasound transducer. However, this would probably only lead to errors in the temperature estimate at the onset of the heating procedure, since the water in between the spheres would act to equalize the temperature over time. This may be one of the factors that cause the temperature differences between the ultrasound-based estimate of the temperature and fiber-optic experimental values for probe 1 at 1.5 min and for probe 2

at 2.3 min. For probe 1, ultrasound-based temperature estimation initially overestimates the temperature at 1.5 min. Then as the heating continues the water may distribute the heat via conduction through the entire scanning width of the transducer such that the initial overestimate is corrected and an underestimation of the temperature is observed for the remainder of the heating. This underestimation of the temperature is probably due to the tip of the fiber-optic probe being displaced or tilted as discussed above. For probe 2, ultrasound-based temperature measurements initially underestimated the temperature at 2.3 min. Following this period, the same process may have occurred as for probe 1, and as the heating continued the ultrasound-based temperature estimate matched that obtained with the fiber-optic temperature probes.

Finally, our temperature estimates suffer from a fairly large standard deviation (up to ± 5 °C). This standard deviation is much larger than that found using other ultrasound-based temperature estimation techniques. For instance, Anand *et al* (2007) demonstrated the ability to track temperatures to within ± 1 °C by tracking the echo shift due to the speed of sound shifts. However, their results were limited to a temperature increase of 10–15 °C. Beyond this range, the effects of thermal expansion have to be accounted for.

Other ultrasound-based temperature estimation techniques, such as frequency shift tracking (Amini *et al* 2005) or measuring the change in the backscattered energy (Arthur *et al* 2005b), also demonstrate smaller standard deviations in their temperature estimates. However, these methods are also only accurate for temperature ranges of $\sim$20 °C. The temperature results presented in this paper may suffer from a higher standard deviation than the aforementioned temperature estimation methods, but it is currently the only method that can accurately track a larger temperature range of $\sim$40 °C (23–65 °C). This temperature range, however, does not represent the entire range of temperatures present during an RF ablation procedure (37–100 °C). However, this is more a limitation of the TM material then of the ultrasound-based temperature estimation method presented in this paper that operate over the entire temperature range for RF ablation (Varghese *et al* 2002, Varghese and Daniels 2004, Techavipoo *et al* 2005). One reason that our temperature estimates may suffer from such a relatively high standard deviation is that although we utilize 2D CC the displacement estimates were noisy, even when a smoothing filter was applied. In future work improved displacement algorithms such as those described by Jiang and Hall (2006) will be evaluated in order to further reduce displacement estimation noise, and thereby the noise and standard deviation of the temperature estimates.

References

Amini A, Ebbini E and Georgiou T 2005 Noninvasive estimation of tissue temperature via high-resolution spectral analysis techniques *IEEE Trans. Biomed. Eng.* **52** 221–8

Anand A, Savery D and Hall C 2007 Three-dimensional spatial and temporal temperature imaging in gel phantoms using backscattered ultrasound *IEEE Trans. Ultrason. Ferroelectr. Freq. Control* **54** 23–31

Arthur R M *et al* 2005a Non-invasive estimation of hyperthermia temperatures with ultrasound *Int. J. Hyperthermia* **21** 589–600

Arthur R M *et al* 2005b Temperature dependence of ultrasonic backscattered energy in motion-compensated images *IEEE Trans. Ultrason. Ferroelectr. Freq. Control* **52** 1644–52

Bosch F X *et al* 2004 Primary liver cancer: worldwide incidence and trends *Gastroenterology* **127** S5–16

Carter D L *et al* 1998 Magnetic resonance thermometry during hyperthermia for human high-grade sarcoma *Int. J. Radiat. Oncol. Biol. Phys.* **40** 815–22

Chin R, Madsen E and Zagzebski J A 1990 A reusable perfusion supporting tissue-mimicking material for ultrasound hyperthermia phantoms *Med. Phys.* **17** 380–90

Clarke R L, Bush N L and Ter Haar G R 2003 The changes in acoustic attenuation due to *in vitro* heating *Ultrasound Med. Biol.* **29** 127–35

Damianou C 2004 MRI monitoring of the effect of tissue interfaces in the penetration of high intensity focused ultrasound in kidney *in vivo Ultrasound Med. Biol.* **30** 1209–15
El-Serag H 2004 Hepatocelluar carcinoma: recent trends in the United States *Gastroenterology* **127** S167–78
Gazelle G S *et al* 2000 Tumor ablation with radio-frequency energy *Radiology* **217** 633–46
Goldberg S N *et al* 1998 Ablation of liver tumors using percutaneous RF therapy *Am. J. Roentgenol.* **170** 1023–8
Greenspan M and Tschegg C 1959 Measurement of the speed of sound in water *J. Acoust. Soc. Am.* **31** 75–6
Hahn P F *et al* 1997 Liver tumor ablation: real-time monitoring with dynamic CT *Acad. Radiol.* **4** 634–8
Head H and Dodd G 2004 Thermal ablation for hepatocelluar carcinoma *Gastroenterology* **127** S159–66
Heisterkamp J, van Hillegersberg R and IJzermans J N 1999 Critical temperature and heating time for coagulation damage: implications for interstitial laser coagulation (ILC) of tumors *Lasers Surg. Med.* **25** 257–62
Hindley J *et al* 2004 MRI guidance of focused ultrasound therapy of uterine fibroids: early results *Am. J. Roentgenol.* **183** 1713–9
Hyodoh H *et al* 1998 Microwave coagulation therapy on hepatomas: CT and MR appearance after therapy *J. Magn. Reson. Imaging* **8** 451–8
Jiang J and Hall T J 2006 A regularized real-time motion tracking algorithm using dynamic programming for ultrasonic strain imaging *2006 IEEE Int. Ultrasonics Symp.*
Madsen E *et al* 1999 Interlaboratory comparison of ultrasonic backscatter, attenuation, and speed measurements *J. Ultrasound Med.* **18** 615–31
Merkle E M *et al* 1999 MRI-guided radiofrequency thermal ablation of implanted VX2 liver tumors in a rabbit model: demonstration of feasibility at 0.2 T *Magn. Reson. Med.* **42** 141–9
Palussiere J *et al* 2003 Feasibility of MR-guided focused ultrasound with real-time temperature mapping and continuous sonication for ablation of VX2 carcinoma in rabbit thigh *Magn. Reson. Med.* **49** 89–98
Simon C, VanBaren P and Ebbini E 1998 Two-dimensional temperature estimation using diagnostic ultrasound *IEEE Trans. Ultrason. Ferroelectr. Freq. Control* **45** 1088–99
Steiner P *et al* 1997 Monitoring of radio frequency tissue ablation in an interventional magnetic resonance environment. Preliminary *ex vivo* and *in vivo* results *Invest. Radiol* **32** 671–8
Techavipoo U, Chen Q and Varghese T 2005 Ultrasonic noninvasive temperature estimation using echoshift gradient maps: simulation results *Ultrason. Imaging* **27** 166–80
Techavipoo U *et al* 2002 Temperature dependence of ultrasonic propagation speed and attenuation in canine tissue *Ultrason. Imaging* **24** 246–60
Techavipoo U *et al* 2004 Temperature dependence of ultrasonic propagation speed and attenuation in excised canine liver tissue measured using transmitted and reflected pulses *J. Acoust. Soc. Am.* **115** 2859–65
Varghese T and Daniels M J 2004 Real-time calibration of temperature estimates during radiofrequency ablation *Ultrason. Imaging* **26** 185–200
Varghese T *et al* 2002 Ultrasound monitoring of temperature change during radiofrequency ablation: preliminary *in vivo* results *Ultrasound Med. Biol.* **28** 321–9
Wacker F K *et al* 2004 MRI-guided radiofrequency thermal ablation of normal lung tissue: *in vivo* study in a rabbit model *Am. J. Roentgenol.* **183** 599–603
Weast R 1978 *CRC Handbook of Chemistry and Physics* 58th edn (Boca Raton, FL: CRC Press) p F-5
Wilson J 2005 Liver cancer on the rise *Ann. Intern. Med.* **142** 1029–32
Worthington A E and Sherar M D 2001 Changes in ultrasound properties of porcine kidney tissue during heating *Ultrasound Med. Biol.* **27** 673–82
Zhu Y and Hall T J 2002 A modified block matching method for real-time freehand strain imaging *Ultrason. Imaging* **24** 161–76